2D Materials

PAPER

Low-loss phase modulation using a MoS_2 monolayer integrated on silicon waveguides

Cheng-Han Wu[1,2,3], Tom Reep[1,2,3], Yishu Huang[1,2], Steven Brems[2], Christian Haffner[2], Cedric Huyghebaert[2], Bart Kuyken[1,2], Joris Van Campenhout[2], Marianna Pantouvaki[2], Dries Van Thourhout[1,2] and Yujie Guo[1,2,*]

[1] Photonics Research Group, Department of information Technology, Ghent University-imec, Technologiepark-Zwijnaarde 15, 9052 Gent, Belgium
[2] Imec, Kapeldreef 75, 3001 Leuven, Belgium
[3] These authors contributed equally to this work.
[*] Author to whom any correspondence should be addressed.

E-mail: Yujie.Guo@UGent.be

Keywords: MoS_2, phase modulator, integrated photonics, silicon photonics, CVD grown TMDC

Supplementary material for this article is available online

OPEN ACCESS

RECEIVED
11 April 2025

REVISED
26 May 2025

ACCEPTED FOR PUBLICATION
30 June 2025

PUBLISHED
16 July 2025

Abstract

Two dimensional (2D) materials are at the forefront of research in integrated modulators. However, achieving pure phase modulation with low insertion loss remains challenging in 2D material modulators. This work explores phase modulators based on monolayer MoS_2 integrated on a Si photonic platform. We investigated the electro-optical response of MoS_2 using two device architectures: a monolayer MoS_2 integrated on a doped Si waveguide and a MoS_2–Al_2O_3–MoS_2 capacitor integrated on an undoped Si waveguide. At a wavelength of 1550 nm, the integration of MoS_2 in both architectures induces minimal optical insertion losses. Specifically, the single-layer device on a doped silicon waveguide achieves a phase modulation efficiency of 0.53 V·cm, with propagation losses dominantly originating from the doped silicon (108 dB cm^{-1}). The MoS_2–Al_2O_3–MoS_2 modulator has a low propagation loss of 6.4 dB cm^{-1} and modulation efficiency of 1 V·cm. Depending on the resistance–capacitance constant, a trade-off exists between achievable modulation efficiency, electro-optical bandwidth, and insertion loss. The strong and lossless electro-refractive response makes MoS_2-based phase modulators suitable for a variety of applications such as light detection and ranging, optical switching, quantum and optical neural networks, and coherent optical communication.

1. Introduction

Two-dimensional (2D) materials have attracted significant interest in integrated photonics due to their superior optoelectronic properties, natural surface passivation, high wafer-scale integration, and compatibility with various photonic platforms. Notably, electro-absorption modulators (EAMs) and photodetectors based on 2D materials have been successfully integrated onto silicon photonic platforms [1–4]. However, an area that remains largely unexplored is their potential for efficient phase modulation. Energy-efficient phase modulators are desired to encode information on an optical carrier for coherent communication schemes (e.g. quadrature amplitude modulation), and to replace energy-inefficient thermal phase shifters in applications such as light detection and ranging (LiDAR), quantum photonics, optical neural networks [5–9].

Graphene has been experimentally demonstrated as a viable material for phase modulation [10, 11]. Due to the gapless Dirac-cone band structure and fast carrier dynamics, graphene-based modulators have achieved high-speed optical communication, with reported 3 dB bandwidths up to 35 GHz [12, 13]. However, a key challenge is that phase modulation in graphene is inherently accompanied by absorption modulation. To minimize the absorption

and thus insertion losses, the graphene modulator is required to operate at a high Fermi level, typically in the transparent region associated with Pauli blocking. However, the reduced mobility of graphene at high carrier concentrations may diminish the speed of the electro-optical response in graphene devices. In defective graphene grown by chemical vapor deposition (CVD), the strong intra-band scattering further increases the insertion loss when operating away from the neutrality point.

Recently, transition metal dichalcogenides (TMDCs), a family of 2D semiconducting materials, have demonstrated potential for efficient phase modulation with minimal optical loss [14, 15]. The most promising candidates are tungsten disulfide (WS_2), tungsten diselenide (WSe_2), and molybdenum disulfide (MoS_2), owing to their tunability of refractive index, both near excitonic resonances and at near-infrared wavelengths. This strong electro-refractive effect has been extensively studied in WS_2 and WSe_2. A WS_2–SiN platform has shown a large doping-induced phase over absorption change ($\frac{\Delta n}{\Delta k}$) of 125. The corresponding Mach–Zehnder interferometer (MZI)-based modulator demonstrated a high modulation efficiency, defined by the voltage length requirement to achieve π phase shift ($V_\pi L$), of 0.8 V·cm [14]. Later, the same group demonstrated a hybrid WSe_2 and graphene modulator integrated on a silicon nitride (SiN) ring resonator, which achieved a $V_\pi L$ of 0.53 V·cm and an electro-optical (EO) bandwidth of 14.8 GHz [15]. In contrast, research on MoS_2-based phase modulators is still in its early stages, with only one experimental report showing a $V_\pi L$ of 1.7 V·cm [14]. MoS_2 is an important member of the TMDC family, with a thickness-dependent bandgap of 1.2–1.8 eV and mobility in excess of 200 cm^2/Vs. The monolithic integration of MoS_2 is advancing rapidly, positioning it as a leading material for applications in nanoelectronics, integrated photonics, 3D integration, electrical interconnects, and sensors [16–18]. As such, exploring MoS_2 phase modulators holds significant scientific and practical potential for future technologies [14, 15].

In this work, we demonstrate MoS_2-based phase modulators integrated with silicon waveguides. Two distinct MoS_2 device configurations are explored: (1) MoS_2 on a doped silicon waveguide, enabling back-gating for electro-optical modulation, and (2) a double-layer MoS_2 modulator on top of a silicon waveguide, used to reduce insertion loss while retaining a strong phase modulation response. The former device achieves a phase modulation efficiency of 0.53 V·cm but with relatively high propagation losses of 108 dB cm^{-1} originating from the doped waveguide. The latter has a modulation efficiency of 1 V·cm and a lower propagation loss of 6.4 dB cm^{-1}. The tunable refractive index and low optical losses of our demonstrated MoS_2 modulators pave the way for energy-efficient and effective optical phase modulators.

2. MoS_2 synthesis, transfer and characterization

The MoS_2 used was grown on a 200 mm sapphire wafer using CVD [19–21]. Utilizing a semi-dry transfer method, the MoS_2 was released from the sapphire substrate using thermal release tape immersed in water. After transferring it to the target substrate, the MoS_2 was dried. The thermal release tape was then removed by heating the entire substrate, followed by a solvent bath process to eliminate any remaining polymer residues. The MoS_2 was patterned into active channels for the waveguide-integrated modulators using e-beam lithography followed by a chlorine (Cl_2) and oxygen (O_2) dry etching process.

Figure 1(a) shows an optical microscope image of a photonic chip covered with patterned MoS_2 nanosheets. Photoluminescence (PL) characterization confirms the successful integration of a monolayer of MoS_2 on the target photonic chip.The well-pronounced PL signal confirms the monolayer nature of the CVD-grown MoS_2 due to its band structure with a direct bandgap. In contrast, multilayer MoS_2 has an indirect bandgap which cannot sustain efficient radiative recombination, resulting in significantly weaker PL signals [22]. In addition, the quality of the transferred MoS_2 is also monitored by means of photoluminescence. As shown in figure 1(b), the as-grown MoS_2 on the sapphire substrate exhibits PL peaks at 1.87 eV and 1.78 eV, corresponding to the monolayer MoS_2 and sapphire, respectively. After transfer to the SiO_2 or Al_2O_3 film on a silicon substrate, the MoS_2 PL peak red-shifts to 1.81 eV and 1.80 eV, respectively. This shift indicates the bandgap narrowing of the transferred MoS_2, which can be attributed to several factors such as selective doping, strain effects, the dielectric environment, and alteration of the surface quality [22, 23].

To characterize the phase-modulation properties of MoS_2-based devices, we integrated them into asymmetric Mach–Zehnder interferometric (AMZI) modulators. These modulators exhibit wavelength-dependent interference patterns, allowing for the evaluation of the electro-optical performance of the integrated MoS_2 modulators. Two distinct types of MoS_2 phase modulators were investigated: (1) a single-layer MoS_2 modulator, in which a monolayer of MoS_2 is integrated on a doped silicon waveguide coated with a 5 nm thick SiO_2 gate, used for electro-optical modulation. (2) a double-layer MoS_2

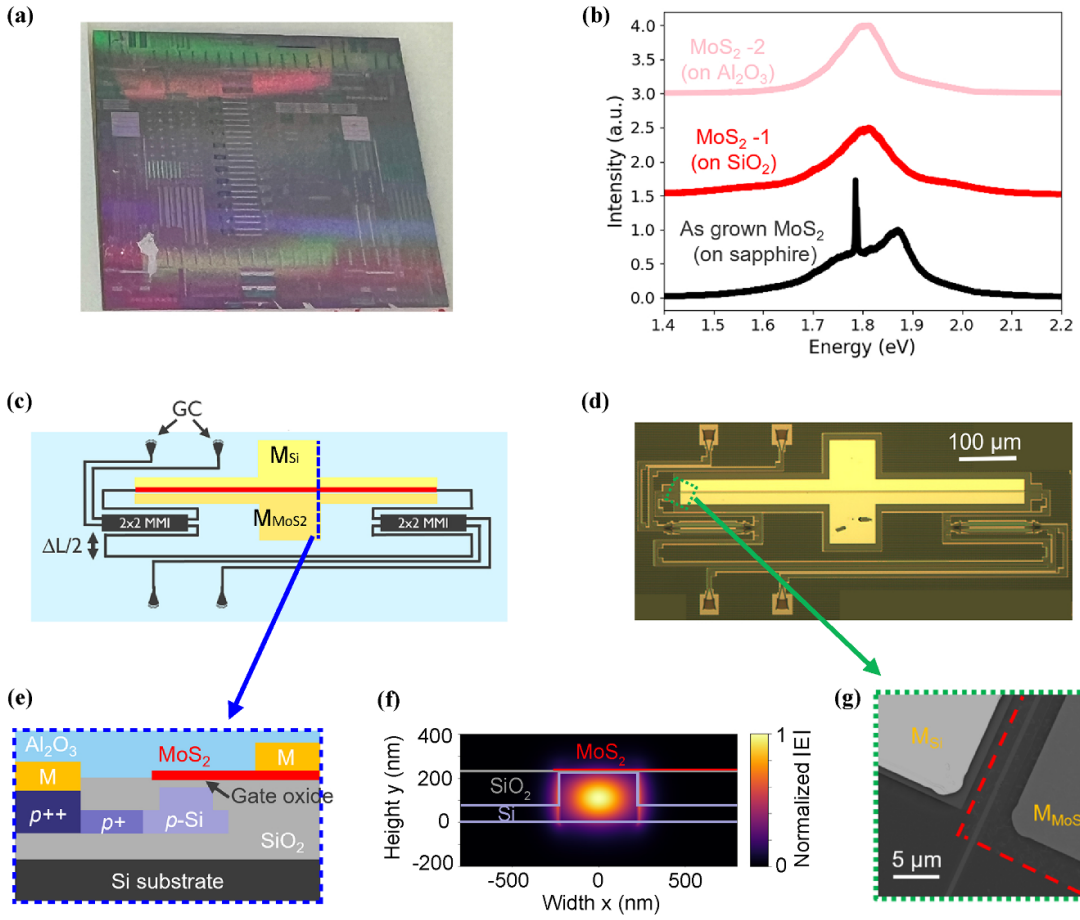

Figure 1. Geometry of the single-layer MoS_2 phase modulator. (a) Photonic chip covered with transferred and patterned MoS_2. (b) Photoluminescence spectra of as-grown MoS_2 on sapphire (black curve), and MoS_2 transferred to a SiO_2 (red curve) or Al_2O_3 (pink curve) layer on a silicon substrate. (c) Schematic of an asymmetric Mach–Zehnder interferometer (AMZI) modulator. (d) Optical microscope image of the AMZI modulator. (e) Cross-section of the single-layer MoS_2 on doped silicon phase modulator. (f) Simulated transverse electric (TE) mode profile which propagates in the Si waveguide. (g) Scanning electron microscope image of the MoS_2 device.

modulator, consisting of a MoS_2–Al_2O_3–MoS_2 capacitor integrated on an undoped Si waveguide.

3. Single layer MoS_2 modulator

The single-layer MoS_2 (SL-MoS_2) modulator is integrated into one arm of a 2 × 2 AMZI, shown in figures 1(c) and (d), while the other arm contains only a strip waveguide. Light is coupled to and from the AMZI using grating couplers, and multi-mode interferometers are used to split and recombine light between the arms of the AMZI. The AMZI interference fringes were designed to have a FSR of 30 nm as shown in figure 2(b).

A schematic cross-section of the SL-MoS_2 modulator is shown in figure 1(e) in which the doped silicon waveguide shown serves both as an optical waveguide and as an electrode to bias the MoS_2 layer. The waveguide has a thickness of 220 nm, a width of 480 nm, and has three increasing doping levels from the waveguide to the contact regions. This configuration optimizes the balance between contact resistance, sheet resistance, and optical propagation losses. Figure 1(f) shows the transverse electric mode propagating in the Si waveguide, as simulated by Lumerical MODE. Its evanescent field overlaps with the monolayer MoS_2 when using a 5 nm-thick gate dielectric, which confirms the light-MoS_2 interaction for phase modulation. It should be noted only the 480 nm wide MoS_2 layer above the waveguide gets modulated through electro-static gating. The part of MoS_2 that gets modulated has a mode overlap of 0.14 %. Figure 1(g) presents a scanning electron microscope image of the fabricated devices showing the transferred MoS_2 layer, a waveguide, a gate oxide, and metal contacts.

3.1. Fabrication of the SL-MoS_2 modulator

The optical circuit was defined on imec's 200 mm silicon photonics platform, consisting of a 220 nm thick silicon on a 2 μm thick oxide insulator layer [24]. To enable the electrical contact, the Si waveguide is partially etched, forming a rib structure with a 70 nm-thick Si slab layer. We employed a three-stage p-type

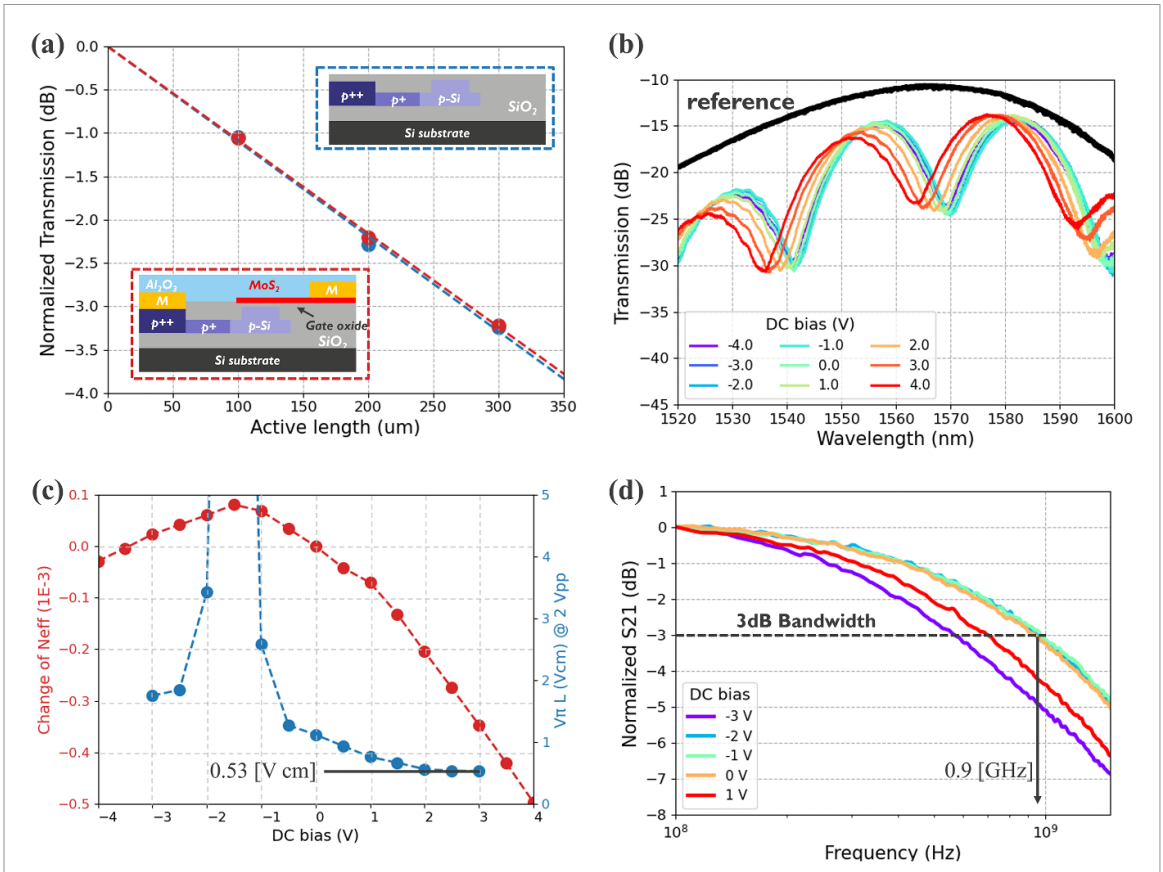

Figure 2. Characterization of the single-layer MoS_2 phase modulator. (a) Propagation loss measurement, with blue markers representing loss measurements before MoS_2 integration and red markers after. (b) Optical transmission of the device when biasing a 600 μm-long phase modulator in one arm. (c) Extracted phase change and $V_\pi L$ of the 600 μm device, assuming a 2 V peak-to-peak voltage. (d) electro-optical modulation speed for a 600 μm long device, showing a $f_{3\,dB}$ bandwidth of 0.9 GHz.

doping process resulting in a highly doped p^{++} for the contact region, p^+ for the slab region, and p-Si at the waveguide core. Following waveguide patterning, chemical mechanical polishing was used to planarize the surface topology to a step variation below 5 nm. A 5 nm thick thermal oxide layer was grown to electrically isolate the MoS_2 from the Si waveguide. Metal contacts to the silicon and MoS_2 were fabricated using e-beam lithography and a metal lift-off process. The metal contact to the MoS_2 layer is composed of a 20 nm Pd on 10 nm Ni stack, while the silicon was contacted with a 30 nm Au on 20 nm Pt on 20 nm Ti metal stack. Before metallization, the thermal oxide layer in the silicon contact region is selectively removed via wet etching in buffered hydrofluoric acid . Finally, the whole chip is encapsulated by a 10 nm Al_2O_3 layer grown by atomic layer deposition (ALD). Supplementary figure A1 provides a schematic of the process flow. The Al_2O_3 layer not only acts as an encapsulation layer to protect the MoS_2, but also influences carrier concentration in MoS_2 through selective doping [22]. Without the Al_2O_3 encapsulation MoS_2 is highly depleted, leading to exhaustion of free carriers. As a result, MoS_2 exhibits high resistance as demonstrated by unstable capacitance voltage measurements in the 1 kHz–1 MHz frequency range (supplementary figure A2). Doping of MoS_2 through the Al_2O_3 layer resolves this issue, significantly improving the device's AC performance.

3.2. Characterization of the SL-MoS_2 modulator

Propagation loss measurements were conducted in the AMZI before and after MoS_2 integration, as shown in figure 2(a). Using the cut-back method, the fitted slope of the dashed lines represents the propagation loss, which are 109 dB cm^{-1} and 108 dB cm^{-1} prior to and after MoS_2 integration, respectively. Thus, the addition of the MoS_2 monolayer did not introduce measurable additional losses. The observed propagation losses are primarily attributed to the doped waveguide. The lowly doped p-Si region in the waveguide core, as described above and illustrated in the insets of figure 2(a), does not induce high propagation losses. In contrast, the p^+-Si in the slab region, with a higher carrier concentration and in close proximity (50 nm) to the waveguide core, is the main contributor to the losses due to strong light scattering. This attribute of losses could be mitigated through further optimization of the

waveguide doping strategy. Alternatively, the possible losses from the MoS_2 monolayer are expected to come from the absorption and scattering occurring at the grain boundaries, surface traps, edge defects and transfer-induced organic residues. The static phase modulation was evaluated by applying a DC voltage between the MoS_2 layer and a 600 μm long doped silicon waveguide, which is integrated into a single arm of an AMZI. The wavelength-dependent transmission of the AMZI under a bias range of −4 V to 4 V is shown in figure 2(b) which clearly shows interference fringes at the designed 30 nm free spectral range (FSR). The lack of change in extinction ratio confirms that biasing does not introduce additional optical losses. The observed shift in interference wavelength when applying a voltage indicates phase shifting. The effective refractive index, and consequently the $V_\pi L$ (assuming a 2 V_{pp} electrical signal), were extracted by tracking the shift in interference wavelength with the applied voltage, as shown in figure 2(c). The optimal result was achieved at a 2.5 V bias, resulting in a $V_\pi L$ of 0.53 V·cm.

The EO modulation speed was characterized by measuring the frequency response of the device using a vector network analyzer , from which the 3 dB EO bandwidth was extracted. The modulation bandwidth varied depending on the carrier state of the p-doped silicon beneath the MoS_2 layer [25]. A 3 dB EO modulation speed of 0.91 GHz was measured at a bias of −1 V for a 600 μm long device, as shown in figure 2(d).

The modulation speed varies depending on DC bias, which aligns with the measured bias-dependent capacitance detailed in supplementary figure A2. Consequently, the device's EO bandwidth is limited by the resistance–capacitance (RC) time constant, influenced by the carrier concentration of the MoS_2 and the p-doped silicon beneath the MoS_2 layer. For a 600 μm long device, a 3 dB electro-optical modulation speed of 0.91 GHz was obtained at a bias of −1 V.

4. Double layer MoS_2 modulator

In order to reduce optical losses, a double-layer MoS_2 (DL-MoS_2) modulator was investigated. This device consists of a MoS_2–Al_2O_3–MoS_2 capacitor structure, with a schematic cross-sectional shown in figure 3(a). Electro-static gating can be achieved by applying a bias between the two MoS_2 layers, eliminating the need for doped waveguides. This reduces optical losses and allows for potential integration on insulator-based platforms such as silicon nitride (SiN) and lithium niobate on insulator (LNOI) [26, 27]. Compared to double-layer graphene modulators, which suffer from high optical insertion losses (around 30 dB cm^{-1}), our MoS_2-based design reduces losses while maintaining a large phase modulation efficiency. However, since MoS_2 has a lower mobility compared to graphene, the EO 3 dB bandwidth is expected to be lower [11].

The DL-MoS_2 modulator was integrated into an AMZI with a 34 μm imbalance, corresponding to a FSR of 10 nm. Figures 3(b) and (c) show a top–down micrograph and a schematic of the AMZI. The double-layer MoS_2 phase modulators with lengths up to 400 μm were integrated into both arms, allowing push-pull operation to further enhance modulation efficiency.

4.1. Fabrication of double layer MoS_2 modulator

The schematic of the process flow of the DL-MoS_2 modulator is shown in supplementary figure A4. The AMZIs was fabricated on imec's 200 mm silicon photonics platform, as described before. Since the silicon waveguide no longer serves as a gate for the MoS_2 layers, fully etched 450 nm-wide waveguides were used in the MoS_2 phase modulation region. The MoS_2 layers were grown and patterned similarly to the single-layer MoS_2 process described in section 2. A 20 nm Pd on 10 nm Ni metal stack was used for electrical contacts. After transferring and defining the first MoS_2 layer, a 10 nm Al_2O_3 gate dielectric was deposited using ALD. The second MoS_2 layer was then transferred and patterned, identically to the first layer. The region where both MoS_2 layers overlap have a width of 750 nm. In this modulated region the bottom MoS_2 layer has an optical mode overlap of 0.17% and the top 0.14%. The DL-MoS_2 device used in this experiment was not encapsulated.

4.2. Characterization of the double layer MoS_2 modulator

The DL-MoS_2 phase modulator exhibited a propagation loss of 6 dB cm^{-1}, which was measured by comparing the transmission of the AMZI structures with varying active lengths (figure 4). This propagation loss is a significant improvement over the SL-MoS_2 modulator (6 dB cm^{-1} vs. 108 dB cm^{-1}) as the DL-MoS_2 device eliminates the loss induced by doped silicon waveguides. In addition to the possible loss from MoS_2, the propagation loss in the DL-MoS_2 modulator also originates from the 10 nm Al_2O_3 gate dielectric.

The phase shift was determined by applying a DC voltage between the two MoS_2 layers of a 400 μm long modulator while keeping the modulator in the other arm shorted. The transmission for various DC voltages, shown in figure 4(b), shows a clear shift in interference wavelength with minimal change in extinction ratio. From these measurements, the change in effective index was extracted for a 2 V peak-to-peak signal from which the $V_\pi L$ was calculated, as shown in figure 4(c). From these calculations an optimal $V_\pi L$ of 1 V·cm was found. The modulation efficiency of the DL-MoS_2 device (0.53 V·cm) is lower than that of the SL-MoS_2 device (1 V·cm), which can

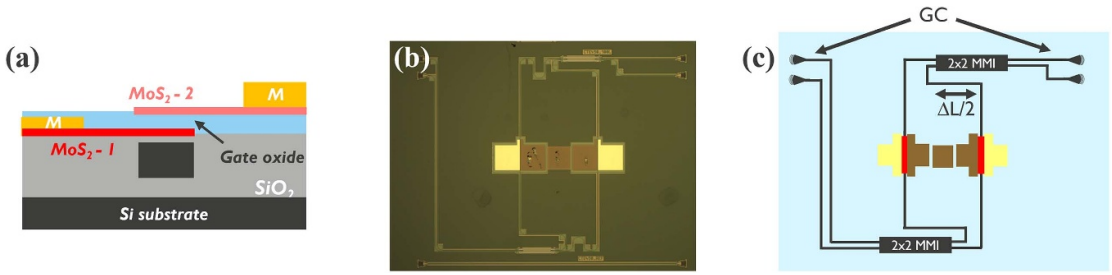

Figure 3. (a) Device architecture of the double-layer MoS_2 modulator. (b) Optical microscope image and (c) scanning microscope image of the device.

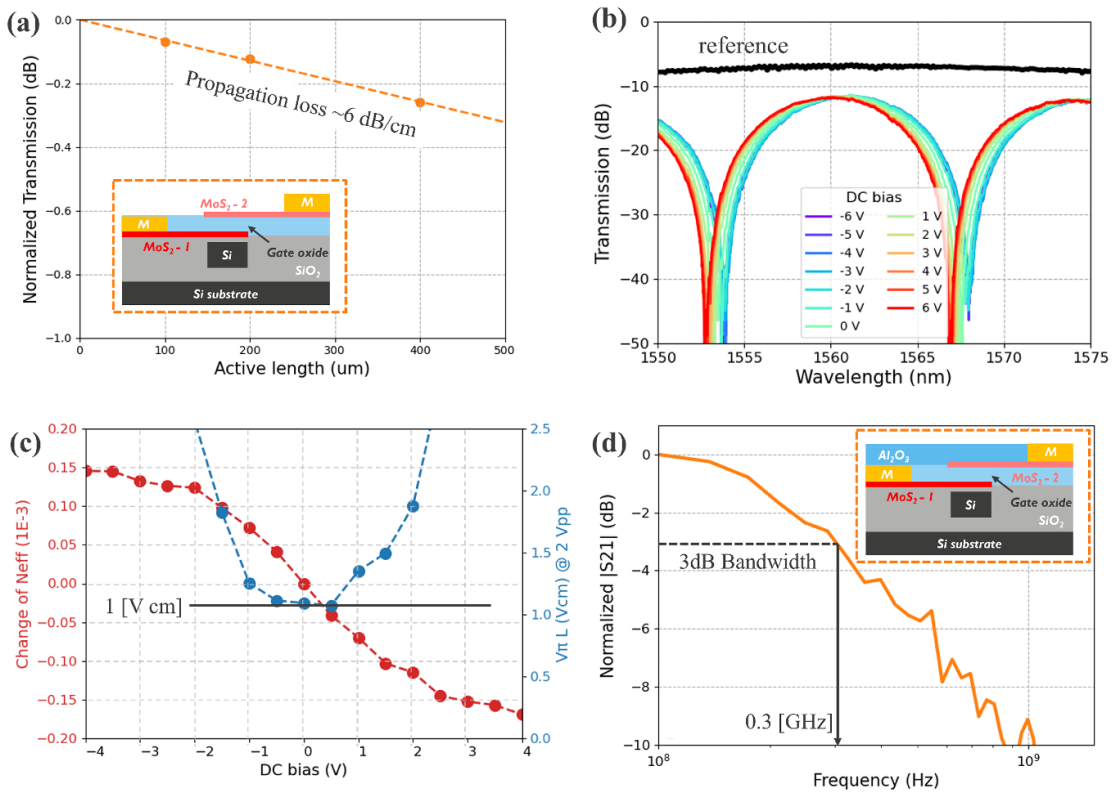

Figure 4. Characterization of the double-layer MoS_2 phase modulator. (a) Propagation loss measurement. (b) Optical transmission of the device when biasing a 400 μm-long phase modulator in one arm. (c) Extracted phase change and $V_\pi L$ of the 400 μm device, assuming a 2 V peak-to-peak voltage. (d) electro-optical modulation speed, showing an f_{3dB} bandwidth of 0.3 GHz.

be attributed to its thicker gate oxide. To evaluate the device property as an efficient phase shifter with low loss, we introduce a phase modulation figure of merit (FoM_{PM}), defined as $FOM_{PM} = \alpha V_\pi L$, where α is the insertion loss. The DL-MoS_2 device achieved an optimal FOM_{PM} of 6.2 dBV, outperforming the SL-MoS_2 modulator (FoM_{PM} = 57.0 dBV) and even Si-based MZI modulators, which typically have an FOM_{PM} in the range of 15 dBV to 22 dBV [28].

The electro-optical response of a 200 μm-long DL-MoS_2 device (figure 4(d)) revealed a f_{3dB} bandwidth of 0.3 GHz. S-parameter analysis in supplementary figure A4 estimated a capacitance of 436 fF and a resistance of 677 Ω, yielding an RC bandwidth of 0.5 GHz, in agreement with experimental data. This electro-optical speed is lower than that of the doped silicon waveguide (0.91 GHz), primarily due to the higher resistance of the MoS_2 gate compared to the doped silicon waveguide.

5. Discussion on MoS_2 based phase modulators

In this work, we demonstrated phase modulators based on MoS_2, exhibiting low propagation losses (6 dB cm^{-1}) and a strong modulation efficiency (as

Table 1. Comparison of phase modulators integrated on a silicon platform.

MZM (references)	oxide thickness (nm)	Loss (dB cm^{-1})	$V_\pi L$ (V cm)	FOM_{PM} (dBV)	Bandwidth (GHz)
Si PIN junction [28]	—	28	2	56	37
Si-oxide-graphene [12]	10	236	0.28	66.1	5
Graphene-oxide-graphene [11]	10	289	0.0954	27.6	4.2
WS_2-oxide-ITO [14]	—	135	0.8	108	0.33
G-O-WSe_2 [15]	45	—	1.08	—	14.9
SL-MoS_2 (this work)	5	100	0.57	57.0	0.91
DL-MoS_2 (this work)	9.5	6.4	0.97	6	0.3

low as 0.53 V·cm), exceeding the performance of other MZI-based phase modulators used on silicon platforms (table 1). Targeting at applications requiring CMOS compatible voltages, we prioritize modulation efficiency over modulation speed. To maximize modulation efficiency, we used a thin gate oxide (5 nm for SL-MoS_2 and 10 nm for DL-MoS_2), ensuring strong electrostatic gating at the cost of increased capacitance (0.3–0.8 μF cm^{-2}). The large capacitance, combined with the inherent high resistivity of MoS_2, limits the EO bandwidth to below 1 GHz. The high modulation efficiency and low optical losses of these devices are advantageous for applications such as LiDAR, laser Doppler vibrometers, optical neural networks, and quantum networks. Additionally, the demonstrated MoS_2 devices are energy-efficient alternatives to thermal phase shifters, which are widely used in optical switches, phased arrays, and tunable lasers.

For certain applications, such as phase modulators used in high-speed coherent communication systems, faster EO modulation speeds tend to be required than that demonstrated by the phase modulators in this work. The EO modulation speed in the MoS_2 modulator can be increased by reducing the capacitance, which can be achieved by increasing the gate oxide thickness which reduces the gate capacitance. As a trade-off, with an increase in gate oxide thickness the modulation efficiency would decrease meaning a higher voltage or longer modulator would be required to reach the same level of phase tuning. An alternative approach is to reduce the device resistance which can be achieved by reducing MoS_2 sheet or contact resistance, or by using an alternative material for gating with a higher conductivity. One recent example of achieving larger EO modulation speeds is a demonstration using a graphene-oxide-WeS_2 modulator which has a 45 nm thick Al_2O_3 gate dielectric to reduce capacitance, and uses a graphene gate to lower device resistance [15]. While this demonstration shows a significant improvement in modulation speed (14.9 GHz at a wavelength of 1646 nm), the modulation efficiency was low with a $V_{\frac{\pi}{2}}$ of 18 V, despite being integrated in a ring resonator with a 20k Q-factor. These required modulating voltages are not CMOS compatible and would require dedicated modulator drivers which come at the cost of increased system complexity and higher power consumption from the driver IC. Furthermore the higher propagation losses arising from the graphene layer results in a total insertion loss of 3.18 dB. Ultimately, the choice of design depends on the application-specific trade-offs between required EO bandwidth, insertion loss, and modulation efficiency or driving voltage requirements.

In addition to the demonstrated capability and flexibility of individual MoS_2 modulators, our study also implies their high potential for scalable photonic integration. The MoS_2 used in the phase modulators was initially grown by CVD on 200 mm sapphire wafers, followed by a semi-dry transfer onto the targeted optical chip. Notably, this semi-dry transfer method has been successfully applied to integrate graphene onto optical waveguides, particularly for EAMs [11]. However, the submersion of the substrate in liquid could lead to unwanted variation in performance of transition metal dichalcogenide based devices, which could be avoided by harnessing dry transfer techniques [29]. These wafer-scale processing demonstrates the feasibility of wafer-scale, CMOS-compatible MoS_2 integration. The ever-growing advances in the MoS_2 growth and transfer methods provide improved channel crystallinity, interface cleanness and device reliability, suggesting a promising path forward for scalable 2D material integration in photonics [18, 30, 31]. Futhermore, ensuring wafer-scale performance and yield also relies on the development of quick and non-destructive characterization techniques over large areas, another critical requirement to realize the promise of 2D materials in integrated photonics [11, 29]. In addition, the stability limitation of MoS_2-based devices has come into focus, particularly when exposed to air and moisture. This issue is mainly caused by oxide defects at the MoS_2/oxide interface, creating charge trapping centres that lead to unwanted hysteresis under gate bias, performance instability and device degradation [32]. Addressing this bottleneck demands optimization of the ALD deposition and encapsulation techniques.

6. Conclusion

This research demonstrates the use of MoS_2 as a promising material for phase modulation on Si photonic waveguides. We explored both SL-MoS_2 and DL-MoS_2 phase modulators integrated in asymmetric MZIs. The electro-optic performance of these modulators is competitive with alternative phase modulators integrated on silicon photonic platforms. The integration of MoS_2 induces minimal losses to the photonic circuit at a wavelength around 1550 nm. The SL-MoS_2 modulator achieves a phase modulation efficiency of 0.53 V·cm with propagation losses primarily originating from the doped silicon (108 dB cm^{-1}). The DL-MoS_2 modulator exhibits a modulation efficiency of 1 V·cm with low propagation losses (6.4 dB cm^{-1}). The devices presented in this paper have oxide thicknesses of less than 10 nm, ensuring a high phase modulation efficiency and EO modulation speeds up to 0.9 GHz. The trade-off between achievable modulation efficiency and EO modulation speed was discussed, highlighting the balance required for different applications. This work contributes to the expanding field of two-dimensional materials-based photonics, demonstrating MoS_2 as a potential material for use in future optical devices and applications.

Data availability statement

All data that support the findings of this study are included within the article (and any supplementary files).

Funding

The author acknowledges funding from the EU Horizon 2020 research and innovation program under Grant Agreement No. 785 219 (Graphene flagship Core2) and No. 881 603 (Graphene flagship Core3) and the European Research Council (ERC) Grant NARIoS under Grant Agreement No. 884 963, ERC Grant CHANSON No. 948 804, and Flanders Research Foundation (FWO) FWO.OPR.2024.0037.01.

Conflicts of interest

The authors declare no conflicts of interest.

References

[1] Agarwal H *et al* 2021 2D-3D integration of hexagonal boron nitride and a high-K dielectric for ultrafast graphene-based electro-absorption modulators *Nat. Commun.* **12** 1070
[2] Goossens S *et al* 2017 Broadband image sensor array based on graphene–CMOS integration *Nat. Photon.* **11** 366–71
[3] Phare C T, Daniel Lee Y-H, Cardenas J and Lipson M 2015 Graphene electro-optic modulator with 30 GHz bandwidth *Nat. Photon.* **9** 511–4
[4] Schuler S *et al* 2021 High-responsivity graphene photodetectors integrated on silicon microring resonators *Nat. Commun.* **12** 3733
[5] Shen Y *et al* 2017 Deep learning with coherent nanophotonic circuits *Nat. Photon.* **11** 441–6
[6] Sun J, Timurdogan E, Yaacobi A, Hosseini E S and Watts M R 2013 Large-scale nanophotonic phased array *Nature* **493** 195–9
[7] Pan B *et al* 2024 III-V-on-Si_3 N_4 widely tunable narrow-linewidth laser based on micro-transfer printing *Photon. Res.* **12** 2508
[8] Tran M A, Huang D, Guo J, Komljenovic T, Morton P A and Bowers J E 2020 Ring-resonator based widely-tunable narrow-linewidth Si/InP integrated lasers *IEEE J. Sel. Top. Quantum Electron.* **26** 1–14
[9] Doylend J K, Heck M J R, Bovington J T, Peters J D, Coldren L A and Bowers J E 2011 Two-dimensional free-space beam steering with an optical phased array on silicon-on-insulator *Opt. Express* **19** 21595–604
[10] Shu H, Su Z, Huang L, Wu Z, Wang X, Zhang Z and Zhou Z 2018 Significantly high modulation efficiency of compact graphene modulator based on silicon waveguide *Sci. Rep.* **8** 991
[11] Wu C, Reep T, Brems S, Yudistira D, Van Campenhout J, Asselberghs I, Huyghebaert C, Pantouvaki M, Wang Z and Van Thourhout D 2024 Graphene-based silicon photonic electro-absorption modulators and phase modulators *IEEE J. Sel. Top. Quantum Electron.* **30** 1–11
[12] Sorianello V, Midrio M, Contestabile G, Asselberghs I, Van Campenhout J, Huyghebaert C, Goykhman I, Ott A K, Ferrari A C and Romagnoli M 2018 Graphene–silicon phase modulators with gigahertz bandwidth *Nat. Photon.* **12** 40–44
[13] Dalir H, Xia Y, Wang Y and Zhang X 2016 Athermal Broadband graphene optical modulator with 35 GHz speed *ACS Photonics* **3** 1564–8
[14] Datta I *et al* 2020 Low-loss composite photonic platform based on 2D semiconductor monolayers *Nat. Photon.* **14** 256–62
[15] Datta I, Gil-Molina A, Chae S H, Zhou V, Hone J and Lipson M 2024 2D material platform for overcoming the amplitude–phase tradeoff in ring resonators *Optica* **11** 48–57
[16] Mannix A J *et al* 2022 Robotic four-dimensional pixel assembly of van der Waals solids *Nat. Nanotechnol.* **17** 361–6
[17] Zhang Y, Tao Li, Yi D, Xu J B and Tsang H K 2020 Enhanced four-wave mixing with MoS_2 on a silicon waveguide *J. Opt.* **22** 025503
[18] Nguyen V L *et al* 2023 Wafer-scale integration of transition metal dichalcogenide field-effect transistors using adhesion lithography *Nat. Electron.* **6** 146–53
[19] Shi Y *et al* 2021 Engineering wafer-scale epitaxial two-dimensional materials through sapphire template screening for advanced high-performance nanoelectronics *ACS Nano* **15** 9482–94
[20] Gaur A, Chiappe D, Lin D, Cott D, Asselberghs I, Heyns M and Radu I 2019 Analysis of admittance measurements of MOS capacitors on CVD grown bilayer MoS_2 *2D Mater.* **6** 035035
[21] Arutchelvan G *et al* 2021 Impact of device scaling on the electrical properties of MoS_2 field-effect transistors *Sci. Rep.* **11** 6610
[22] Leonhardt A, Chiappe D, Afanas'ev V V, El Kazzi S, Shlyakhov I, Conard T, Franquet A, Huyghebaert C and Gendt S 2019 Material-selective doping of 2D TMDC through AlxOy encapsulation *ACS Appl. Mater. Interfaces* **11** 42697–707

[23] Leonhardt A *et al* 2020 Use of the Indirect Photoluminescence Peak as an Optical Probe of Interface Defectivity in MoS_2 *Adv. Mater. Interfaces* **7** 2000413
[24] Absil P P, Verheyen P, De Heyn P, Pantouvaki M, Lepage G, De Coster J and Van Campenhout J 2015 Silicon photonics integrated circuits: a manufacturing platform for high density, low power optical I/O's *Opt. Express* **23** 9369–78
[25] Alessandri C, Asselberghs I, Brems S, Huyghebaert C, Van Campenhout J, Van Thourhout D and Pantouvaki M 2020 High speed graphene-silicon electro-absorption modulators for the O-band and C-band *Jpn. J. Appl. Phys.* **59** 052008
[26] Liu J, Huang G, Wang R N, He J, Raja A S, Liu T, Engelsen N J and Kippenberg T J 2021 High-yield, wafer-scale fabrication of ultralow-loss, dispersion-engineered silicon nitride photonic circuits *Nat. Commun.* **12** 2236
[27] Churaev M *et al* 2023 A heterogeneously integrated lithium niobate-on-silicon nitride photonic platform *Nat. Commun.* **14** 3499
[28] Sobu Y, Simoyama T, Tanaka S, Tanaka Y and Morito K 2019 70 Gbaud Operation of all–silicon Mach–Zehnder modulator based on forward–biased PIN diodes and passive equalizer *2019 24th OptoElectronics and Communications Conf. (OECC) and 2019 Int. Conf. on Photonics in Switching and Computing (PSC)* pp 1–3
[29] Asselberghs I *et al* 2020 Wafer-scale integration of double gated WS_2-transistors in 300mm Si CMOS fab *2020 IEEE Int. Electron Devices Meeting (IEDM)* (IEEE)
[30] Liu L, Cai Z, Xue S, Huang H, Chen S, Gou S, Zhang Z, Guo Y, Yao Y and Bao W 2025 A mass transfer technology for high-density two-dimensional device integration *Nat. Electron.* **8** 135–46
[31] Jiang H *et al* 2025 Two-dimensional Czochralski growth of single-crystal MoS_2 *Nat. Mater.* **24** 188–96
[32] Illarionov Y Y *et al* 2024 Process implications on the stability and reliability of 300 mm FAB MoS_2 field-effect transistors *npj 2D Mater. Appl.* **8** 8